



PHANGS–JWST First Results: Multiwavelength View of Feedback-driven Bubbles (the Phantom Voids) across NGC 628

Ashley. T. Barnes^{1,2}, Elizabeth J. Watkins³, Sharon E. Meidt⁴, Kathryn Kreckel³, Mattia C. Sormani⁵, Robin G. Treß⁶, Simon C. O. Glover⁵, Frank Bigiel¹, Rupali Chandar⁷, Eric Emsellem^{2,8}, Janice C. Lee⁹, Adam K. Leroy^{10,11}, Karin M. Sandstrom¹², Eva Schinnerer¹³, Erik Rosolowsky¹⁴, Francesco Belfiore¹⁵, Guillermo A. Blanc^{16,17}, Médéric Boquien¹⁸, Jakob den Brok¹, Yixian Cao¹⁹, Mélanie Chevance^{5,20}, Daniel A. Dale²¹, Oleg V. Egorov³, Cosima Eibensteiner²², Kathryn Grasha^{23,24}, Brent Groves²⁵, Hamid Hassani¹⁴, Jonathan D. Henshaw^{13,26}, Sarah Jeffreson²⁷, María J. Jiménez-Donaire²⁸, Benjamin W. Keller²⁹, Ralf S. Klessen^{5,30}, Eric W. Koch²⁷, J. M. Diederik Kruijssen²⁰, Kirsten L. Larson³¹, Jing Li³, Daizhong Liu¹⁹, Laura A. Lopez^{10,11,32}, Eric J. Murphy³³, Lukas Neumann¹, Jérôme Pety^{34,35}, Francesca Pinna¹³, Miguel Querejeta²⁸, Florent Renaud³⁶, Toshiki Saito³⁷, Sumit K. Sarbadhicary^{10,11}, Amy Sardone¹⁰, Rowan J. Smith³⁸, Sophia K. Stuber¹³, Jiayi Sun^{39,40}, David A. Thilker⁴¹, Antonio Usero²⁸, Bradley C. Whitmore⁴², and Thomas G. Williams^{13,43}

¹ Argelander-Institut für Astronomie, Universität Bonn, Auf dem Hügel 71, D-53121, Bonn, Germany; ashleybarnes.astro@gmail.com

² European Southern Observatory, Karl-Schwarzschild-Straße 2, D-85748 Garching, Germany

³ Astronomisches Rechen-Institut, Zentrum für Astronomie der Universität Heidelberg, Mönchhofstraße 12-14, D-69120 Heidelberg, Germany

⁴ Sterrenkundig Observatorium, Universiteit Gent, Krijgslaan 281 S9, B-9000 Gent, Belgium

⁵ Universität Heidelberg, Zentrum für Astronomie, Institut für Theoretische Astrophysik, Albert-Ueberle-Straße 2, D-69120 Heidelberg, Germany

⁶ Institute of Physics, Laboratory for Galaxy Evolution and Spectral Modelling, EPFL, Observatoire de Sauverny, Chemin Pegais 51, 1290 Versoix, Switzerland

⁷ Ritter Astrophysical Research Center, University of Toledo, Toledo, OH 43606, USA

⁸ Univ Lyon, Univ Lyon1, ENS de Lyon, CNRS, Centre de Recherche Astrophysique de Lyon UMR5574, F-69230 Saint-Genis-Laval, France

⁹ Gemini Observatory/NSF's NO iRLab, 950 N. Cherry Avenue, Tucson, AZ 85719, USA

¹⁰ Department of Astronomy, The Ohio State University, 140 West 18th Avenue, Columbus, OH 43210, USA

¹¹ Center for Cosmology and Astroparticle Physics, 191 West Woodruff Avenue, Columbus, OH 43210, USA

¹² Department of Physics, University of California, San Diego, 9500 Gilman Drive, San Diego, CA 92093, USA

¹³ Max-Planck-Institut für Astronomie, Königstuhl 17, D-69117 Heidelberg, Germany

¹⁴ Department of Physics, University of Alberta, Edmonton, AB, T6G 2E1, Canada

¹⁵ INAF-Arcetri Astrophysical Observatory, Largo E. Fermi 5, I-50125, Florence, Italy

¹⁶ The Observatories of the Carnegie Institution for Science, 813 Santa Barbara St., Pasadena, CA 91101, USA

¹⁷ Departamento de Astronomía, Universidad de Chile, Camino del Observatorio 1515, Las Condes, Santiago, Chile

¹⁸ Centro de Astronomía (CITEVA), Universidad de Antofagasta, Avenida Angamos 601, Antofagasta, Chile

¹⁹ Max-Planck-Institut für Extraterrestrische Physik (MPE), Giessenbachstr. 1, D-85748 Garching, Germany

²⁰ Cosmic Origins Of Life (COOL) Research DAO, coolresearch.io

²¹ Department of Physics and Astronomy, University of Wyoming, Laramie, WY 82071, USA

²² Argelander-Institut für Astronomie, Universität Bonn, Auf dem Hügel 71, D-53121 Bonn, Germany

²³ Research School of Astronomy and Astrophysics, Australian National University, Canberra, ACT 2611, Australia

²⁴ ARC Centre of Excellence for All Sky Astrophysics in 3 Dimensions (ASTRO 3D), Australia

²⁵ International Center for Radio Astronomy Research, University of Western Australia, 7 Fairway, Crawley, 6009 WA, Australia

²⁶ Astrophysics Research Institute, Liverpool John Moores University, 146 Brownlow Hill, Liverpool, L3 5RF, UK

²⁷ Center for Astrophysics, Harvard & Smithsonian, 60 Garden Street, Cambridge, MA 02138, United States

²⁸ Observatorio Astronómico Nacional (IGN), C/Alfonso XII, 3, E-28014 Madrid, Spain

²⁹ Department of Physics and Materials Science, University of Memphis, 3720 Alumni Avenue, Memphis, TN 38152, USA

³⁰ Universität Heidelberg, Interdisziplinäres Zentrum für Wissenschaftliches Rechnen, Im Neuenheimer Feld 205, D-69120 Heidelberg, Germany

³¹ AURA for the European Space Agency (ESA), Space Telescope Science Institute, 3700 San Martin Drive, Baltimore, MD 21218, USA

³² Flatiron Institute, Center for Computational Astrophysics, NY 10010, USA

³³ National Radio Astronomy Observatory, 520 Edgemont Road, Charlottesville, VA 22903, USA

³⁴ IRAM, 300 rue de la Piscine, 38400 Saint Martin d'Hères, France

³⁵ LERMA, Observatoire de Paris, PSL Research University, CNRS, Sorbonne Université, 75014, Paris

³⁶ Department of Astronomy and Theoretical Physics, Lund Observatory, Box 43, SE-221 00 Lund, Sweden

³⁷ National Astronomical Observatory of Japan, 2-21-1 Osawa, Mitaka, Tokyo, 181-8588, Japan

³⁸ Jodrell Bank Centre for Astrophysics, Department of Physics and Astronomy, University of Manchester, Oxford Road, Manchester, M13 9PL, UK

³⁹ Department of Physics and Astronomy, McMaster University, 1280 Main Street West, Hamilton, ON, L8S 4M1, Canada

⁴⁰ Canadian Institute for Theoretical Astrophysics (CITA), University of Toronto, 60 St George Street, Toronto, ON, M5S 3H8, Canada

⁴¹ Department of Physics and Astronomy, The Johns Hopkins University, Baltimore, MD 21218, USA

⁴² Space Telescope Science Institute, 3700 San Martin Drive, Baltimore, MD 21218, USA

⁴³ Sub-department of Astrophysics, Department of Physics, University of Oxford, Keble Road, Oxford, OX1 3RH, UK

Received 2022 October 17; revised 2022 November 17; accepted 2022 November 29; published 2023 February 16

Abstract

We present a high-resolution view of bubbles within the Phantom Galaxy (NGC 628), a nearby (~ 10 Mpc), star-forming ($\sim 2 M_{\odot} \text{ yr}^{-1}$), face-on ($i \sim 9^\circ$) grand-design spiral galaxy. With new data obtained as part of the Physics at High Angular resolution in Nearby Galaxies (PHANGS)-JWST treasury program, we perform a detailed case



Original content from this work may be used under the terms of the [Creative Commons Attribution 4.0 licence](#). Any further distribution of this work must maintain attribution to the author(s) and the title of the work, journal citation and DOI.

study of two regions of interest, one of which contains the largest and most prominent bubble in the galaxy (the Phantom Void, over 1 kpc in diameter), and the other being a smaller region that may be the precursor to such a large bubble (the Precursor Phantom Void). When comparing to matched-resolution H α observations from the Hubble Space Telescope, we see that the ionized gas is brightest in the shells of both bubbles, and is coincident with the youngest (~ 1 Myr) and most massive ($\sim 10^5 M_\odot$) stellar associations. We also find an older generation (~ 20 Myr) of stellar associations is present within the bubble of the Phantom Void. From our kinematic analysis of the H I, H₂ (CO), and H II gas across the Phantom Void, we infer a high expansion speed of around 15 to 50 km s $^{-1}$. The large size and high expansion speed of the Phantom Void suggest that the driving mechanism is sustained stellar feedback due to multiple mechanisms, where early feedback first cleared a bubble (as we observe now in the Precursor Phantom Void), and since then supernovae have been exploding within the cavity and have accelerated the shell. Finally, comparison to simulations shows a striking resemblance to our JWST observations, and suggests that such large-scale, stellar-feedback-driven bubbles should be common within other galaxies.

Unified Astronomy Thesaurus concepts: Superbubbles (1656); Stellar feedback (1602); Interstellar medium (847); Infrared astronomy (786)

1. Introduction

High-mass stars ($> 8 M_\odot$) are fundamental in driving the evolution of galaxies, due to the large amounts of energy and momentum (i.e., stellar feedback) that they inject into the interstellar medium (ISM) during their short lifetimes (e.g., Krumholz et al. 2014). At early times (< 5 Myr), feedback in the pre-supernova (pre-SN) stages of high-mass stars (i.e., within H II regions) plays a critical role in disrupting molecular clouds and forming bubbles within the ISM (e.g., Dale et al. 2012, 2013; Raskutti et al. 2016; Gatto et al. 2017; Rahner et al. 2017; Grasha et al. 2018; Kim et al. 2018; Grasha et al. 2019; Hannon et al. 2019; Rahner et al. 2019; Kannan et al. 2020; Barrera-Ballesteros et al. 2021a, 2021b; Kim et al. 2021b; Barnes et al. 2021; Jeffreson et al. 2021; McLeod et al. 2021; Chevance et al. 2022a; Barnes et al. 2022; Hannon et al. 2022). At later times, these bubbles can merge (Clarke & Oey 2002; Simpson et al. 2012; Krause et al. 2015), and feedback from supernovae (SNe) can further act to drive expansion, forming so-called (super)bubble structures with scales of tens to thousands of parsecs over timescales of tens of millions of years (e.g., McKee & Ostriker 1977; Mac Low & McCray 1988; Oey & Clarke 1997; Weisz et al. 2009a, 2009b; Bagetakos et al. 2011; Keller et al. 2014, 2015, 2016; Kruijssen et al. 2019; Chevance et al. 2020; Nath et al. 2020; Kim et al. 2021a; Chevance et al. 2022b; Kim et al. 2022b; Orr et al. 2022; Zucker et al. 2022), even driving fountains out of the galactic plane (e.g., Veilleux et al. 2005; Fraternali 2017).

With the advent of the JWST, we can now, for the first time, achieve the resolution, sensitivity, and coverage for an unprecedented view of bubble populations within galaxies beyond the Milky Way and the Local Group. Specifically, the wavelength coverage of the Mid-Infrared Instrument (MIRI) is perfectly suited to this task, as it is sensitive to several polycyclic aromatic hydrocarbon (PAH) emission features (e.g., at 7.7 μm ; see Draine & Li 2007; Smith et al. 2007; Li 2020). Emission from PAHs is particularly useful in tracing the shells of feedback-driven bubbles (e.g., Pineda et al. 2022), due to (a) the increased gas densities found in swept-up shells (PAHs are generally well mixed with the gas and illuminated by the average interstellar radiation field such that they trace the gas column very sensitively; e.g., Regan et al. 2006; Leroy et al. 2013; Chown et al. 2021; Gao et al. 2022; Leroy et al. 2023), (b) the high number of ionizing photons emitted by the OB association powering the bubbles, leading to PAHs being destroyed in the photoionized interiors of the bubbles (e.g., Galliano et al. 2018; Chastenet et al. 2023a, 2023b;

Egorov et al. 2023), and (c) the low optical depth from the shell interior to the edge, which will allow far-UV photons to easily heat the small dust grains (e.g., Draine & Li 2007; Draine 2011; Hensley & Draine 2021). Together, these cause the edges of bubbles to appear with high contrast against their interior PAH emission (e.g., Churchwell et al. 2006; Watson et al. 2008).

In a companion Letter in this Issue, Watkins et al. (2023) use a combination of JWST and Hubble Space Telescope (HST) observations to study the bubble population across the nearby (9.84 ± 0.63 Mpc; Anand et al. 2021a, 2021b), star-forming ($1.8 \pm 0.5 M_\odot \text{ yr}^{-1}$), face-on ($i \sim 9^\circ$; Lang et al. 2020, and also see Blanc et al. 2013), massive ($M_* = 10^{10.3} M_\odot$, $M_{\text{H I}} = 10^{9.7} M_\odot$, $M_{\text{H}_2} = 10^{9.4} M_\odot$; Walter et al. 2008; Querejeta et al. 2015; Leroy et al. 2019, 2021a), spiral galaxy Messier 74 (also known as NGC 628 or the Phantom Galaxy). These authors manually identify bubbles using a combination of 7.7 μm JWST-MIRI observations (Lee et al. 2023), B-band (438 nm) Physics at High Angular resolution in Nearby Galaxies (PHANGS)-HST observations (Lee et al. 2022), and Very Large Telescope (VLT)-Multi Unit Spectroscopic Explorer (MUSE) H α observations (Emsellem et al. 2022). For each bubble, Watkins et al. (2023) fit circular or elliptical apertures to the bubble boundaries (i.e., the shells) seen within this multiwavelength data set, and in doing so identify ~ 1700 bubbles with radii ranging between 6 and 500 pc (e.g., left panel of Figure 1). These structures are clearly pervasive across the galaxy, form a complex nested structure (where smaller bubbles are preferentially located at the edges of large bubbles), and are among the most striking features in the initial JWST images (see Watkins et al. 2023 for an in-depth discussion of the nesting of these structures and their size distributions).

In the Watkins et al. (2023) catalog, one hole stands out due to its size (over ~ 1 kpc in diameter), circular shape, and strong contrast with respect to its environment (e.g., right panel of Figure 1). We refer to this impressive feature as the Phantom Void, which is the focus of this Letter (Table 1 summarizes the main properties of the Phantom Void that have been determined within this work). To help understand this structure, we also identify a nearby more compact, but still very well-defined bubble, which we call the Precursor Phantom Void and analyze in parallel (also see Table 1). To conduct our analysis, we combine all the data sets available taken as part of the PHANGS⁴⁴-JWST survey (Lee et al. 2023) and existing PHANGS multiwavelength observations to assemble a

⁴⁴ <http://www.phangs.org>

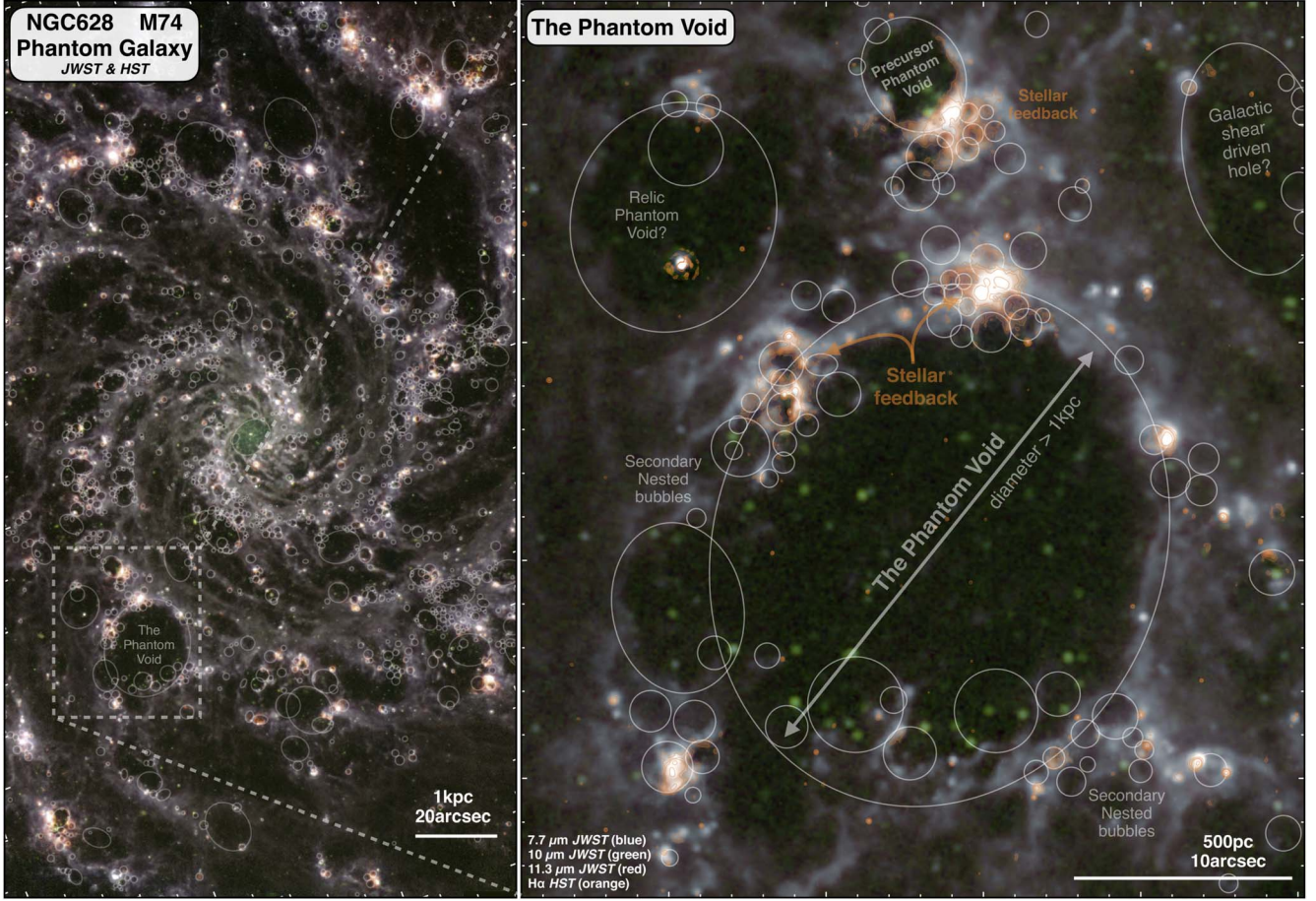


Figure 1. The prominent bubble structures across the Phantom Galaxy (Messier 74 or NGC 628). In all panels, we show an image produced from the 770W (blue), 1000W (green), and 1130W (red) band filters from the JWST (Lee et al. 2023), and overlaid in orange is the continuum-subtracted HST H α . The faded circles and ellipses show the positions of the bubbles from Watkins et al. (2023).

Table 1
Properties of the Phantom Void and the Precursor Phantom Void

Property	The Phantom Void		Precursor	
	Bubble	Shell	Bubble	Shell
R.A. (deg)	24.1866	24.1864	24.1863	24.1863
Decl. (deg)	15.7719	15.7719	15.7784	15.7782
r_{major} (arcsec)	10.8	17.6	1.7	4.9
r_{minor} (arcsec)	4.5	16.0	1.3	4.3
r_{pa} (deg)	126	126	30	30
r_{mean} (pc)	364	801	69	219
$M_{\text{H}_2} (M_{\odot}/10^5)$	12.8	379.9	3.1	38.0
$M_{\text{H}_1} (M_{\odot}/10^5)$	7.0	56.4	0.2	3.5
$M_{*} (M_{\odot}/10^5)$	1.8	7.8	1.4	1.4
$\Sigma_{\text{H}_2} (M_{\odot} \text{ pc}^{-2})$	3.7	22.8	20.6	28.1
$\Sigma_{\text{H}_1} (M_{\odot} \text{ pc}^{-2})$	2.1	3.4	2.4	2.6
$v_{\text{exp}} (\text{km s}^{-1})$	~ 20		~ 6	

Note. Tabulated are the properties of the bubble (i.e., the ellipsoid central cavity) and shell (i.e., the ellipsoid annulus around the cavity) of each source (shown in Figure 2). We present the central position, the semimajor and semiminor axis length, and the position angle of the ellipse used to define the outer boundary of the bubbles and shells, and, also, the mean radius of these ellipses in units of parsec. We also present the total molecular (Section 3.2.1) and atomic (Section 3.2.2) hydrogen masses and mass surface densities, and total stellar mass in young stellar associations (derived from the association catalog of Deger et al. 2020 and Larson et al. 2023; see Section 3.3). Lastly, we show an estimate of the expansion velocity (Section 3.2).

complete panchromatic, multiphase picture of the gas, stars, and dust in these bubbles.

2. Observations

2.1. PHANGS–JWST Observations

The PHANGS–JWST observations were taken as part of the Cycle 1 treasury project ID 02107 (Lee et al. 2023), which targets 19 nearby, star-forming galaxies with the Near Infrared Camera (F200W, F300M, F335M, and F360M) and MIRI (F770W, F1000W, F1130W, and F2100W) imaging. The observations targeting NGC 628 cover the main star-forming disk (containing 50% of the total star formation of the galaxy), which is matched to coverage from Hubble (Lee et al. 2022), VLT-MUSE (Emsellem et al. 2022), and the Atacama Large Millimeter/submillimeter Array (ALMA; Leroy et al. 2021a). We primarily make use of the F770W filter observations in this work, which have a point-spread function (PSF) FWHM of $\sim 0.^{\prime\prime}25$ (~ 12 pc at the galaxy distance). A detailed description of the complete data reduction is presented in Lee et al. (2023).

2.2. Hubble Space Telescope Observations

We make use of near-UV (NUV) *UBVI*-band HST observations taken from the LEGUS survey (Calzetti et al. 2015) and reduced using the PHANGS–HST survey pipeline

(see Lee et al. 2022). The PSF of these observations have a FWHM of $\sim 0''.1$ – $0''.2$ (~ 5 – 10 pc). In addition, we use the narrowband F658N map from the HST to produce a higher resolution ($\sim 0''.1$) $H\alpha$ emission map (Proposal 10402). To do so, the F658N map is continuum-subtracted using an image formed from a combination of the F814W and F550M maps, appropriately scaled using their AB zero points (see Hannon et al. 2022 for methods).⁴⁵

In this Letter, we also include the properties (e.g., ages and masses; Section 3.3) taken from the stellar association catalog (Deger et al. 2020; Lee et al. 2022; Larson et al. 2023). The properties in this catalog were determined from spectral energy distribution modeling of the HST broadband filters with CIGALE (Boquien et al. 2019) based on Bruzual & Charlot (2003) single stellar populations, while also including ionized gas emission (lines and continuum) and dust attenuation. We make use of the *B*-band selected catalog with an association scale of 32 pc (Larson et al. 2023). For this work, using a catalog selected from a different band or association over a different scale makes no significant difference to our results.

2.3. Ancillary Observations

We also make use of continuum-subtracted emission line maps ($H\alpha$ [$O\,I$]6300, [$S\,II$]6716) and line kinematics based on VLT/MUSE observations from the PHANGS–MUSE survey (see Emsellem et al. 2022 for a complete discussion of the processing and reduction of these observations). These provide a higher sensitivity yet lower resolution ($\sim 1''$) view of the ionized gas compared to the HST $H\alpha$ map, better suited to identifying the diffuse emission within bubbles. In addition, we use CO (2–1) observations from the PHANGS–ALMA survey (see Leroy et al. 2021a for a complete description of the survey and Leroy et al. 2021b for the processing and reduction of the data), a NUV emission map from Astrosat (Hassani et al. 2023), a $8\,\mu m$ map from Spitzer (Kennicutt et al. 2003; Dale et al. 2009), and natural-weighted HI observations from the Very Large Array (VLA) THINGS survey (Walter et al. 2008). We conduct our analysis by using a common astrometric grid, retaining the native resolution of our multiwavelength data sets to preserve information (as opposed to smoothing to a common resolution).

3. Blowing Bubbles

3.1. A Detailed Look at Feedback Bubbles

Figure 2 presents a detailed, multiwavelength view of the Phantom Void and the Precursor Phantom Void regions. In the Phantom Void, we see that the main bubble is relatively devoid of any JWST $7.7\,\mu m$ emission (values of $<1\,MJy\,sr\,pix^{-1}$) or HST $H\alpha$ emission (values of $<10^{-17}\,erg\,s^{-1}\,cm^{-2}\,arcsec^{-2}$) toward the central cavity, and emission is discretely distributed around the bubble shell. We note that we use this nomenclature throughout this Letter, where “bubble” refers to the inside cavity, while the “shell” refers to the perimeter with some thickness (as labeled on Figure 2). Comparing to the broadband NUV HST and Astrosat observations, we find that many of these emission peaks in the shell are connected to compact stellar emission sources (discussed further in Section 3.3).

⁴⁵ We are not correcting the narrowband flux for the contribution of the [$N\,II$] emission lines. This has no impact on the results presented in this Letter as we are primarily interested in the morphology of the emission rather than its absolute brightness.

When comparing to the high-sensitivity, but lower resolution, PHANGS–MUSE observations, we see that there is a low-level component to the diffuse $H\alpha$ emission inside of the bubble. This emission could be connected to the more diffuse emission seen in broadband HST and Astrosat observations, and is consistent with ionization by an older generation of stars (with respect to those associated with compact $H\alpha$ emission in the shell).

In contrast, the Precursor Phantom Void appears to be associated with a single star-forming complex (seen in $H\alpha$ and NUV emission) located at the edge of the shell. Moreover, there is clear evidence from the HST observations that the ionizing radiation is propagating through the bubble and illuminating its far edge, which appears bright in $H\alpha$ emission. Low-level $H\alpha$ is also seen in the higher sensitivity MUSE observations within the bubble cavity. Additionally, it appears that there are many more compact and less evacuated secondary bubbles toward the south of the region, which are associated with bright extended $H\alpha$ emission.

Together, the structures seen in the Phantom Void and the Precursor Phantom Void suggest that the bubbles we are seeing in the JWST imaging are driven by multiple generations of high-mass stars, the youngest of which are located at the bubble edges (see Section 4 for a discussion of, for example, trigger star formation). These stars are then injecting their ionizing radiation into the bubble, which must have a relatively low density of hydrogen such that the radiation can propagate through the bubble and cause the diffuse $H\alpha$ emission at the dusty shell boundary. Specifically, for a characteristic ionizing photon energy of 20 eV, we expect the optical depth of a 100 pc bubble with mean atomic hydrogen density n_H to be approximately $\tau \sim 500(n_H/cm^{-3})$, implying that n_H cannot be larger than $\sim 0.01\,cm^{-3}$.⁴⁶ That said, the Phantom Void is even larger than this, so could have an even lower density. Indeed, the Phantom Void is so large that it is even visible as a hole within comparatively low-resolution HI observations (~ 500 pc beam; Walter et al. 2008), confirming a low atomic hydrogen density within its evacuated center (see Figure 2). Given that the estimated HI disk scale height of NGC 628 is ~ 800 pc (Dutta et al. 2008), roughly the size of the the Phantom Void, it has likely burst out of the galaxy. Bubbles on this scale are one mechanism that could be responsible for shaping galactic-scale chimneys (Heiles 1984) and establishing gas recycling via galactic fountains (e.g., Fraternali 2017). An interesting avenue for the future would be to investigate if this cavity is filled with outflowing hot X-ray gas (e.g., with Chandra).

3.2. Bubble Expansion

We aim to measure the expansion speed of the bubbles with a number of independent methods using our multiwavelength data sets. These are summarized in the following subsections.

3.2.1. Molecular Gas

We make two estimates of the expansion velocity from the CO (2–1) data (Leroy et al. 2021a). First, we make an estimate using the line width measured inside of the bubble, which probes the motion out of the plane (i.e., a difference between faint emission at the front and back side of the bubble). Second,

⁴⁶ Here we make the assumption that all the gas is atomic. However, it could be possible that some of the gas is ionized, which would lower the atomic gas optical depth and allow for a higher density.

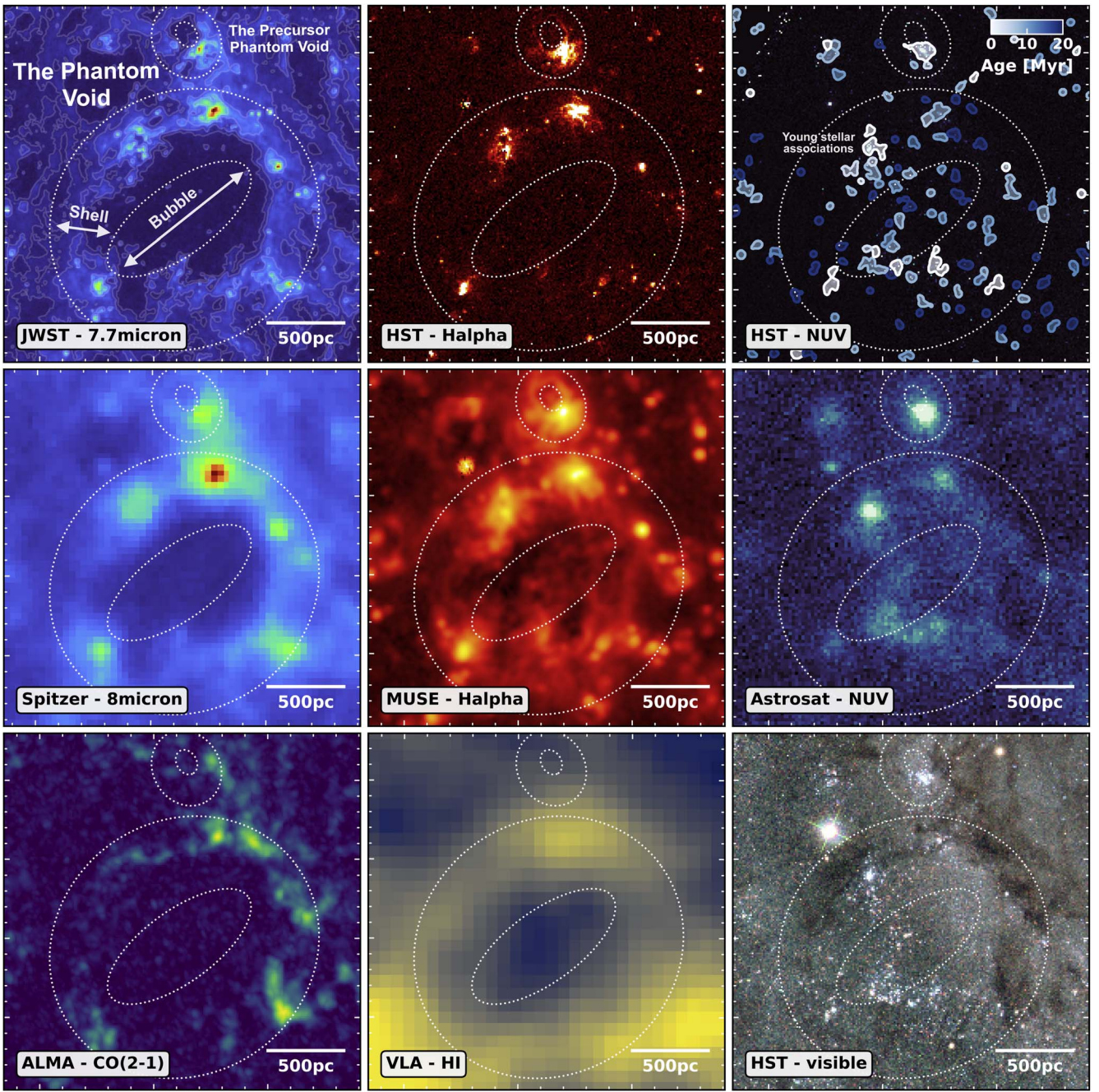


Figure 2. Comparison of a feedback-driven bubble and its host stellar population for the Phantom Void and the Precursor Phantom Void (also shown in Figure 1). From left to right in upper panels, we show the JWST 7.7 μm , HST H α , and the NUV (F275W) filters. Overlaid as colored contours on the upper-right panel is the age of the stellar associations (at a scale of 32 pc; see Deger et al. 2020). From left to right in the center panels are the Spitzer 8 μm (Dale et al. 2009), MUSE H α (Emsellem et al. 2022), and Astrosat NUV (Hassani et al. 2023) observations. In the bottom panels are the ALMA CO (Leroy et al. 2021a), VLA HI (Walter et al. 2008), and HST broadband (Lee et al. 2022) observations. The white dashed line in all panels denotes the bubble and shell of each region (see Figure 7). We find that young and high-mass stellar associations (<20 Myr; $>10^5 M_{\odot}$) exist within the bubble (particularly toward the boundaries), highlighting these as good candidates for driving the bubble expansion.

we make an estimate using the velocity of the emission in the shell of the bubble, which probes the motion in the direction of the galactic plane.

In Figure 3, we show the average CO (2–1) spectrum taken from inside of both bubbles, which show a weak, yet significant, signal. Here, we use a data cube that has had the local velocity field subtracted, including projected circular and noncircular motions, and, hence, the signal is centered on $\sim 0 \text{ km s}^{-1}$. We fit the emission with a Gaussian function, and measure a FWHM of 31.9 km s^{-1} for the Phantom Void and

12.1 km s^{-1} for the Precursor Phantom Void. We make the assumption that this line width is the result of the line-of-sight component of the approaching and receding side of the bubble shell.⁴⁷ Assuming spherical expansion, then, $v_{\text{exp}} = \text{FWHM}/2 \sim 16 \text{ km s}^{-1}$ for the Phantom Void and ~ 6

⁴⁷ We note, however, that for large bubbles of the order of galactic-scale heights, such as the Phantom Void, the bubble expansion deforms into a prolate spheroid perpendicular to the galaxy disk. This can affect the measured expansion velocity with respect to the expansion in the plane of the galaxy (see, e.g., Baumgartner & Breitschwerdt 2013).

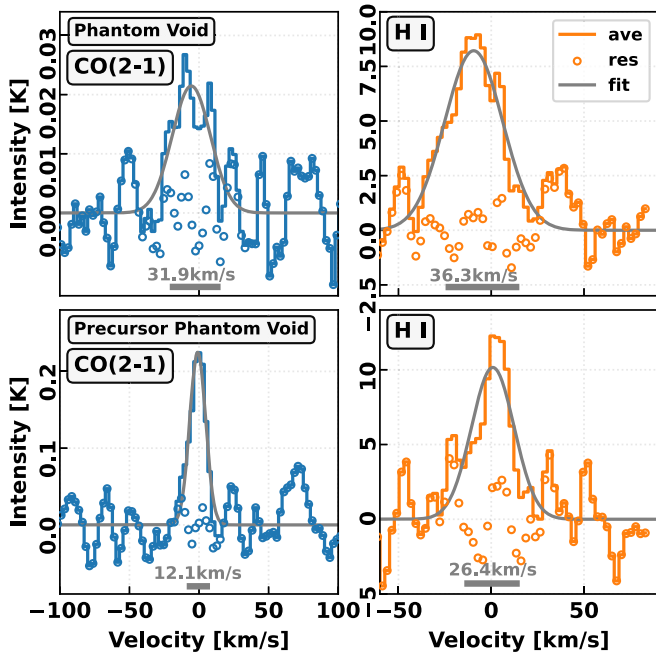


Figure 3. Spectra taken inside of the Phantom Void bubble (see Figure 2). In the left and right panels, we present the average CO (2–1) spectrum obtained from the cube that has had the local velocity field subtracted (including rotational and nonrotational components) and the average H I spectrum, respectively. Gaussian fits to the data are overlaid as gray curves. Residuals are plotted as open points. Below each curve, we show a bar and text showing the measured FWHM (corrected for the instrument spectral resolution).

km s⁻¹ for the Precursor Phantom Void, where the expansion velocity here is the difference in velocity between the receding and approaching side of the bubble out of the plane.

In Figure 4, we show the molecular gas velocity field that highlights local, noncircular flows in the galactic plane at the location of the Precursor Phantom Void. Focusing on the centroid velocity of the emission around the bubble, we find that residual velocities are negative on the left side of the shell and positive on the right side of the shell. Given the orientation, rotation direction and inclination of NGC 628, this would correspond to expansion outward from the center of the bubble (i.e., the left part of the shell is moving toward a larger galactocentric radius and the right part of the shell is moving toward a smaller galactocentric radius). Specifically, from Figure 4 we measure that the v_{resid} on the left part of the bubble is ~ -5 km s⁻¹, whereas on the right part of the bubble it is $+3$ km s⁻¹, with a few positions at $+5$ km s⁻¹. This would give $|v_{\text{resid}}| \sim 3\text{--}5$ km s⁻¹, and hence we estimate that for the Phantom Void $v_{\text{exp}} = |v_{\text{resid}}|/\sin(i) = 20\text{--}35$ km s⁻¹ (where $i = 8.9^\circ$; Lang et al. 2020; see also Blanc et al. 2013).

Given the simplistic assumptions on the geometry of the system, we consider that these estimates of the expansion speed perpendicular and parallel to the plane of the galaxy are consistent for the Phantom Void. Hence the expansion velocity of the molecular gas is taken to be in the range $v_{\text{exp}} \sim 5\text{--}35$ km s⁻¹. As the Precursor Phantom Void is located within the spiral arm, and due to its smaller size relative to the the Phantom Void, there is more confusion in separating the bubble from the surrounding gas within the residual velocity map. Hence, the in-plane expansion speed of the Precursor Phantom Void cannot be estimated, and we take the expansion speed estimate from the out-of-plane method: $v_{\text{exp}} \sim 6$ km s⁻¹.

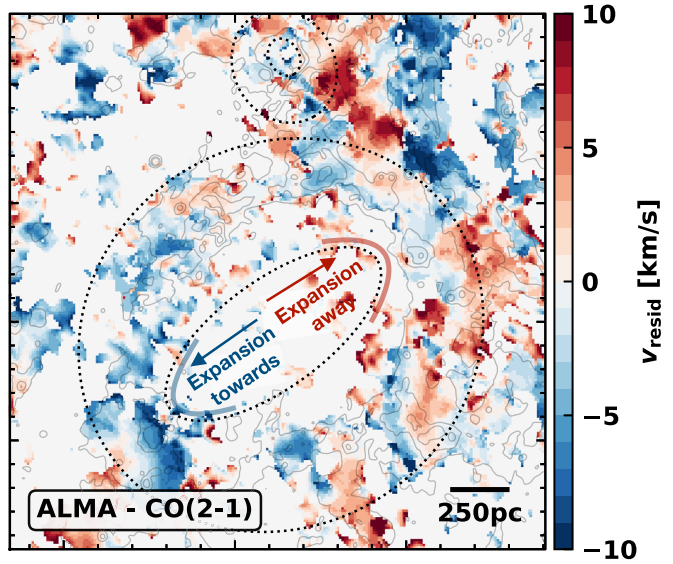


Figure 4. Residual CO velocity toward the voids. Here we show the local, nonrotational flows at the location of the phantom void, constructed from the intensity-weighted centroid velocity map after subtracting the projected rotational velocity (measured by Lang et al. 2020) from each pixel. Overlaid as black contours on each panel is the 7.7 μm emission (see Figure 2).

3.2.2. Atomic Gas

To constrain the expansion speed in the neutral gas, we use the VLA H I (natural-weighted) data cube (Figure 2). As with the CO (2–1), we measure the averaged spectrum for the center of the Phantom Void bubble (Figure 3, right panel), and again fit the emission with a Gaussian function. We measure a FWHM of 36.3 km s⁻¹, which is very similar to the estimate obtained from the CO (32.4 km s⁻¹). This gives a $v_{\text{exp}} = \text{FWHM}/2 \sim 18$ km s⁻¹.

For completeness, we also estimate the atomic gas expansion speed of the Precursor Phantom Void using the same method. We measure a FWHM = 26.4 km s⁻¹, giving $v_{\text{exp}} \sim 13$ km s⁻¹. This estimate should, however, be taken with caution, as the beam size of the VLA is larger than the size of the Precursor Phantom Void bubble, and, hence, could include a significant contribution from gas kinematics outside of the bubble.

3.2.3. Ionized Gas

We use the MUSE H α emission line kinematics to constrain the expansion speed in the ionized gas (Figure 5, left panels). Across the same region used to measure the molecular and atomic expansion speeds, we find that the average FWHM for the Phantom Void is 88.4 km s⁻¹ ($v_{\text{exp}} \sim 45$ km s⁻¹).⁴⁸ Similarly, we find a FWHM for the Precursor Phantom Void of 85.1 km s⁻¹ ($v_{\text{exp}} \sim 45$ km s⁻¹). These values are significantly higher than what is measured in the neutral gas ($\sim 6\text{--}20$ km s⁻¹), even when accounting for the larger thermal contribution to the FWHM of the warmer ionized medium (e.g. ~ 20 km s⁻¹ at 10^4 K), which could highlight the fact that the ionized medium is more directly connected to the source of feedback.

Interestingly, we find systematically elevated line widths in the interior of both bubbles relative to their shells, and even

⁴⁸ The velocity dispersion shown in Figure 5 has been corrected for the instrumental velocity dispersion (Emsellem et al. 2022), and converted to the FWHM (factor of $\sqrt{8\ln(2)}$).

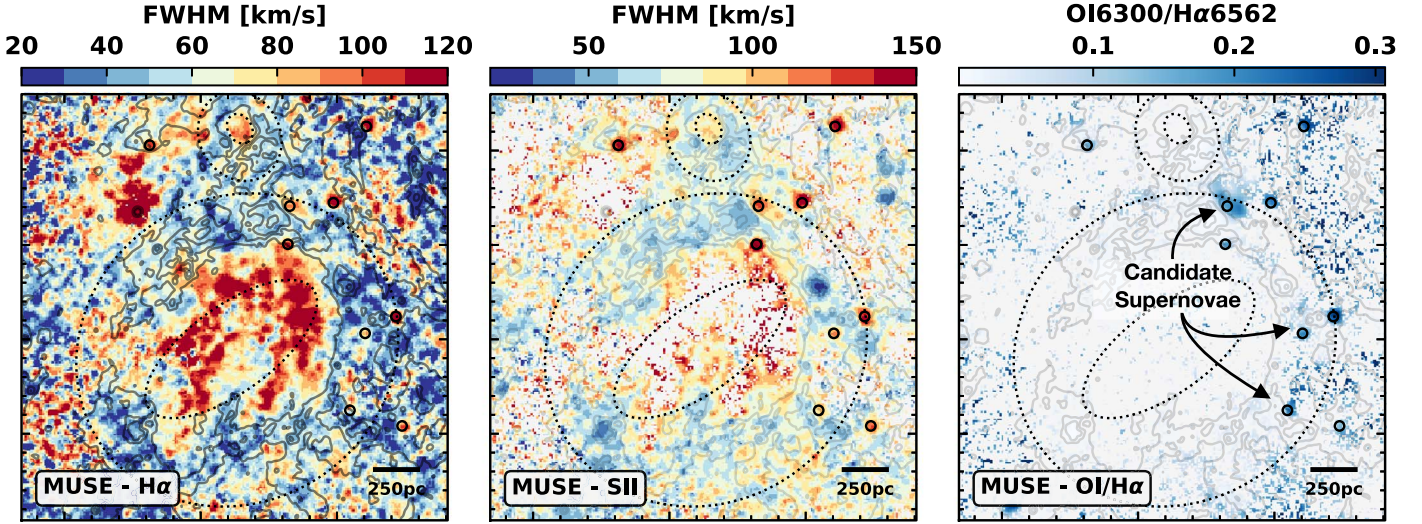


Figure 5. Evidence of stellar feedback in the ionized gas tracers toward the voids. From left to right, we show the emission-weighted velocity FWHM maps from the H α and the [S II]6716 lines, and the emission line ratio [O I]6300/H α . Overlaid as black contours on each panel is the 7.7 μm emission (see Figure 2). We see elevated line widths distributed throughout the center of the bubble (albeit at low signal-to-noise), which we attribute to turbulence and out-of-plane expansion. Moreover, as highlighted on each panel, we see elevated line widths ($>100 \text{ km s}^{-1}$) and line ratios toward the shell, which could be indicative of young SN remnants (J. Li et al. 2022, in preparation).

measure FWHM values of more than 100 km s^{-1} in the Phantom Void (though at these very low signal-to-noise ratios < 10 note there is a bias toward overestimating line widths). Such high values of the line width could be indicative of SN feedback contributing to increased turbulence within the center of the bubble (Egorov et al. 2023). Near the shell, we directly identify SN remnants via their broadened [S II]6716 line emission and increased [O I]/H α line ratios (Figure 5; J. Li et al. 2022, in preparation). The presence of SN explosions within the shell could be contributing to continued driving of the bubble expansion (Section 3.3).

3.2.4. Galactic Dynamical Constraints

In the presence of differential rotation or “rotation curve shear,” expanding structures will become distorted over time (Palous et al. 1990). Here we use the ellipticity, ϵ , of shells of a given radius to place rough constraints on their expansion velocity. Assuming an isotropic bubble expansion velocity, v_{\exp} , and bubble radius, $R_b = \int_0^t v_{\exp} dt$ (in the absence of shear), after bubble age t , the axis ratio ($q = 1 - \epsilon$) of shearing bubbles can be written

$$q = \left(1 + \frac{dV_c}{dR} t_b\right)^{-1} = \left(1 + \frac{dV_c}{dR} \langle R_b \rangle\right)^{-1}, \quad (1)$$

in terms of the rotation curve derivative dV_c/dR , the average (time-weighted) bubble radius,

$$\langle R_b \rangle = \frac{\int_0^t R_b dt}{t}, \quad (2)$$

the average (time-weighted) bubble expansion velocity,

$$\langle v_{\exp} \rangle = \frac{R_b}{t} = \frac{\int_0^t v_{\exp} dt}{t}, \quad (3)$$

(as would be estimated from the present-day size and age), and effective bubble age as estimated by $t_b = \langle R_b \rangle / \langle v_{\exp} \rangle = \langle R_b \rangle / R_{bt}$.

Using Equation (1), the v_{\exp} required to generate bubbles with a given set of average sizes and ellipticities can be determined, provided that the rotation curve is known, that is,

$$\langle v_{\exp} \rangle = \frac{dV_c}{dR} \langle R_b \rangle \left(\frac{1}{q} - 1 \right)^{-1}. \quad (4)$$

Below we use this expression to obtain a basic estimate of v_{\exp} under the assumption of negligible time evolution in the bubble expansion rate, such that the current bubble radius is a good approximation of $\langle R_b \rangle$. Other assumptions for the time evolution of v_{\exp} will yield different results, but this should be useful for illustration purposes.⁴⁹

The Phantom Void, with a radius $R_b \sim 500 \text{ pc}$, sits at $R_{\text{gal}} \sim 2.5 \text{ kpc}$ and has a low ellipticity corresponding to $q \sim 0.85$. Figure 6 shows the expansion velocities that would be required for an expanding structure with these properties to retain such a high degree of circularity. Here we have adopted an analytical two-parameter model for this galaxy’s rotation curve to estimate the rotation curve shear at all locations (Lang et al. 2020). To produce a structure like the Phantom Void, we estimate expansion velocities $v_{\exp} \sim 20 \text{ km s}^{-1}$ are required.

3.2.5. Mass and Energy of the Shell

We use the CO (2–1) ALMA observations to estimate that there is $3.8 \times 10^7 M_{\odot}$ of molecular gas within the shell of the Phantom Void ($1.3 \times 10^6 M_{\odot}$ inside the bubble). Here we use the same shell mask shown in Figure 2, adopt a CO (2–1)/CO (1–0) ratio of 0.61 based on direct observations (den Brok et al. 2021), and a $\alpha_{\text{CO}(1-0)} = 3.93 M_{\odot} \text{ pc}^{-2} (\text{km s}^{-1})^{-1}$ as predicted by empirical scaling relations (Sun et al. 2020). In

⁴⁹ For expansion that declines over time, $\langle v_{\exp} \rangle$ will overestimate the present-day expansion velocity. For example, in the event of an exponentially decreasing v_{\exp} with time, i.e., $v_{\exp}(t) = v_0 e^{-t/t_0}$ with characteristic time t_0 , then when the evolution is fast and $t_0 \ll t$, the stalled radius R_b is well approximated by $\langle R_b \rangle \sim v_0 t_0 \sim R_b$ and the expansion velocity measured from Equation (4) $\langle v_{\exp} \rangle = v_0 t_0 / t = R_b / t$ exceeds the present-day v_{\exp} but is representative of the expansion near its fastest.

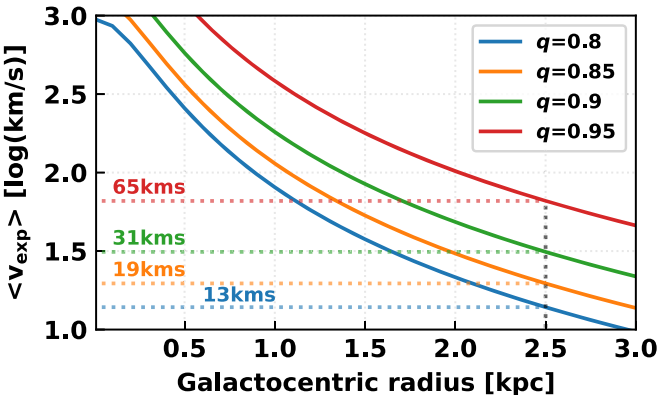


Figure 6. The expansion velocity required for Phantom Void-sized shells to retain a high degree of circularity as they expand in the presence of differential rotation at different locations in the inner disk of NGC 628. Curves show the v_{exp} required for different observed axis ratios $q = 0.8$ to 0.95 (in steps of 0.05). Here a bubble radius $R_b = 500$ pc is adopted and NGC 628’s rotation curve is modeled with a two-parameter fit to the measured rotation curve (Lang et al. 2020). Highlighted are the results corresponding to the approximate galactocentric radius of the Phantom Void.

addition, we estimate that there is $5.6 \times 10^6 M_\odot$ of atomic gas within the shell of the Phantom Void ($7.0 \times 10^5 M_\odot$ inside the bubble), when using the VLA data and the conversion presented in Bigiel et al. (2010).

When taking a representative expansion speed determined in the previous section of $v_{\text{exp}} \sim 20 \text{ km s}^{-1}$, we calculate that the energy required to drive a shell with this combined atomic and molecule mass is $1.7 \times 10^{53} \text{ erg}$. We find the total ($\text{H}_1 + \text{H}_2$) mass inside the shell of the Precursor Phantom Void is about 10 times less than the shell ($4.2 \times 10^6 M_\odot$), which—when assuming an estimated expansion speed of $v_{\text{exp}} \sim 6 \text{ km s}^{-1}$ —implies a kinetic energy of $\sim 10^{51} \text{ erg}$.

A plausible energy source for these bubbles is stellar feedback (as discussed further in the following section). For example, a typical value for the amount of kinetic energy released per SN is $\sim 10^{51} \text{ erg}$ (see, e.g., Bethe 1990; Draine 2011), and, hence, approximately 100 SNe would be required to power the Phantom Void. On the other hand, the Precursor Phantom Void could be powered by a single SN. However, it is worth noting that this number could vary significantly depending on, for example, the contribution from pre-SN feedback (e.g., in the form of winds, which over the lifetime of a high-mass star have been suggested to provide an energy contribution similar to a SN; e.g., Chevance et al. 2022a), and coupling efficiency of these feedback mechanisms with the expanding bubble (e.g., values of the amount of kinetic energy retained in the surrounding medium, and not radiated away, ranges between a few to a few ten percent; e.g., Thornton et al. 1998; Tamburro et al. 2009; Sharma et al. 2014; Kim & Ostriker 2015; Martizzi et al. 2015; Gentry et al. 2017). We estimate the mass of a stellar association required to produce these number of SNe assuming $f_{*-\text{SN}}/\langle m \rangle \sim 0.01$, or that one SN is produced per $100 M_\odot$ of stars that fully populate an initial mass function (see Tamburro et al. 2009). Hence, we estimate that the Phantom Void should contain $> 10^4 M_\odot$ of stars with ages less than a few 10 Myr (i.e., the timescale for the stars to explode as SNe after they are formed), and the Precursor Phantom Void $> 10^2 M_\odot$. As we show in the following section, these criteria are fulfilled.

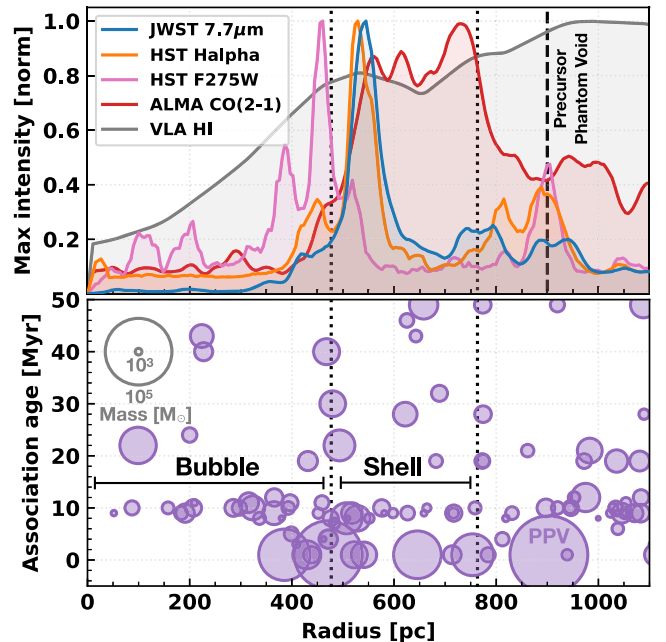


Figure 7. Distribution of intensity and stellar population in the Phantom Void (see Figure 2). The upper panel shows the intensity distribution of the JWST $7.7 \mu\text{m}$, continuum-subtracted $\text{H}\alpha$ emission, HST NUV, ALMA CO, and VLA H I emission, as measured radially from the center of the bubble (see Figure 2). We show the 99th percentile of the intensity in each radial bin, normalized to the value of the maximum bin (this percentile is chosen instead, e.g., the mean value to better highlight where the emission distributions peak). The bottom panel shows the radial age distribution of the stellar association catalog. The size of the points indicate the mass of the stellar associations. In both panels we highlight the position of the the Precursor Phantom Void. We find evidence that younger and more higher mass clusters are preferentially located within the shell, with respect to inside the bubble.

3.3. Stellar Populations Driving Bubbles

Within the Phantom Void, we find many compact and bright concentrations of NUV bright (young) stellar point sources within the shell (see HST F275W filter in Figure 2), which spatially correspond to regions of bright $\text{H}\alpha$ and $7.7 \mu\text{m}$ emission. In addition, there appears to be an overabundance (with respect to a similar-size interarm region adjacent to the bubble) of fainter point sources distributed throughout the bubble cavity, which is also seen as diffuse emission in the AstroSat NUV map.

Figure 7 (upper panel) shows the flux distribution of the JWST $7.7 \mu\text{m}$, HST $\text{H}\alpha$, HST NUV (F275W) filter, ALMA CO, and VLA H I emission maps measured radially from the center of the Phantom Void. We find a good correspondence between the $7.7 \mu\text{m}$ and $\text{H}\alpha$ emission, which both peak within the shell radius at ~ 600 pc (compare to dashed circles in Figure 2). We also see that the HST NUV (F275W) emission is fainter within the bubble. Interestingly, we find that the peak in the NUV emission is at a smaller (~ 100 pc) radius to the $7.7 \mu\text{m}$ and $\text{H}\alpha$ emission, hinting that these clusters may have already evacuated their immediate environment of dense atomic gas and ionized gas, respectively. We also see that the neutral gas tracers (CO and H I emission) are increased within the shell. The Precursor Phantom Void, on the other hand, shows a single compact cluster of point sources in the shell (again correspondent with bright $\text{H}\alpha$ and $7.7 \mu\text{m}$ emission), and very little point-source emission within the bubble.

In Figure 2 (upper-right panel), we also overlay as colored contours the ages of the stellar associations (see Section 2.2; Deger et al. 2020; Larson et al. 2023). These indicate that the stellar associations throughout the bubble and shell are generally young (<20 Myr). We estimate the total stellar mass of these young stellar associations within the the Phantom Void region to be $10^{6.0} M_{\odot}$ (80% of this stellar mass is in the shell and 20% is in the bubble). These associations could be viable powering sources for these bubbles, either currently or, in the case of those inside the bubble of the Phantom Void, they may represent the past generation of stars that created the bubbles (Section 4).

Interestingly, several of the stellar associations are very young (<5 Myr). Both in the Phantom Void and the Precursor Phantom Void, these associations reside in the shells (as inferred from the H α). Indeed, Figure 7 (lower panel) shows the radial distribution of ages from the association catalog across the Phantom Void, where the size of each point indicates the stellar mass. We see evidence that there is a higher number of younger and more massive associations situated within the shell, as opposed to inside of the bubble. We find that there are 10 associations with ages less than 5 Myr within the shell of the Phantom Void, which have a maximum mass of $10^5 M_{\odot}$ (total mass of $3.2 \times 10^5 M_{\odot}$), and, therefore, are massive enough to harbor OB stars (i.e., strong sources of stellar feedback).

We consider whether the stellar population ages align with the previous estimates of the bubble expansion speed. To test this, we make a calculation of the expansion velocity based on the radius of the bubble ($R \sim 500$ pc), and a mean age of the associations within the bubble $t \sim 10$ Myr. According to the classical Weaver et al. (1977) model of expanding bubbles, $v_{\text{exp}} \simeq 0.6R/t$, assuming they are in an adiabatic stage of their evolution. This implies $v_{\text{exp}} = 30 \text{ km s}^{-1}$, which is very close to the values estimated from our kinematic analysis (Section 3.2).

The large size, high expansion speed, and large energy required to power the the Phantom Void bubble (Section 3.2) suggests that the driving mechanism is stellar feedback, sustained by a combination of multiple mechanisms. We propose that early feedback first cleared a bubble, as we are now currently witnessing for the Precursor Phantom Void (and to some extent continue to see in the shell of the Phantom Void). Since then, SNe have been exploding within the cavity and have accelerated the shell (e.g., Keller et al. 2022). This sustained injection of energy and momentum is what is required to reach high (50 km s^{-1}) expansion speeds (i.e., seen in the ionized gas), because the continuous energy input keeps the pressure in the bubble high, whereas having only a single SN would cause the pressure to drop as the bubble expands (e.g., Mac Low & McCray 1988). Finally, the star formation and SNe that are observed in the shell could further contribute to the current and future expansion of the shell.

4. Star Formation at the Bubble Boundaries

We have found that the Phantom Void contains a significant amount of ongoing star formation within its shell (as seen in the H α emission and the young, massive stellar associations), and also that this shell contains a large reservoir of molecular gas (see Table 1). This could then imply several physical scenarios as to why star formation is preferentially located toward the shell, of which we provide an nonexhaustive list of examples below:

- (i) Gravitationally unbound gas is collected in the shell of the bubble as it expands, which then becomes dense and then star formation is triggered (i.e., gas that would not have otherwise formed stars; e.g., Elmegreen & Lada 1977; Whitworth et al. 1994).
- (ii) Gravitationally bound gas either from the parent cloud or surrounding the initial star-forming region is moved by the expansion of the bubble into the shell, which then forms stars (i.e., gas that would have otherwise formed stars but in a different location).
- (iii) If star formation proceeds sequentially in a cloud/region in an inside-out fashion, then we would naturally get the oldest stars in the middle of the cloud, with younger stars near the edge.

Differentiating between these cause-and-effect scenarios for the formation of the feedback-driven bubbles and future episodes of star formation is nontrivial, and has been a very long-standing problem in the galactic star formation community. Nonetheless, below we outline methods to test this in future work.

The different cases make different predictions regarding the ages of the various young stellar clusters/associations. In scenario (i), where star formation is triggered by shell collapse, we would expect all of the young regions in the shell to have ages less than the age of the shell (and hence also less than the age of the central associations). However, this need not be the case in scenario (ii). If bound clouds are being swept up that are already capable of forming stars, then it is likely that some of them will already have stars when they get swept up, whereas others will not, and we would therefore expect to see a broader distribution of ages than in scenario (i).

Another interesting test would be to look at whether there is a population of young stellar clusters/associations just inside the shell. This is what one might expect if the expanding shell sweeps away molecular clouds that have already started forming stars, as the shock will act on the gas but not the stars, which should therefore get left behind. This would be much harder to bring about in scenario (i), as in this case we would expect that the radial outward velocity of the stars at their birth should be the same as that of their parent giant molecular clouds (i.e., they should move along with the shell, or even move out faster than the shell in the case where it is significantly decelerating). Interestingly, as seen in Figure 7, we do find that the young stars (seen in the HST NUV and in the cluster association catalog) are preferentially located on the inner edge of the shell (offset from the peak in $7.7 \mu\text{m}$ emission by 50 to 100 pc).

5. Are Phantom Voids Common in Galaxies?

The Phantom Void is one of the most striking features within the new JWST data, which was not as pronounced in our existing PHANGS multiwavelength data sets. Only with the resolution and sensitivity afforded by JWST do such coherent, large-scale features become clearly apparent (Figure 1). It is then interesting to consider if phantom voids are a common feature of other galaxies.

Watkins et al. (2023) estimates that there should be ~ 1900 bubbles identifiable in the PHANGS–JWST observations per $1 M_{\odot} \text{ yr}^{-1}$ of star formation rate (Section 3.1). Hence, using their size distribution, we expect to find ~ 1 with a radius ~ 500 pc per $1 M_{\odot} \text{ yr}^{-1}$ of star formation rate. This is more or

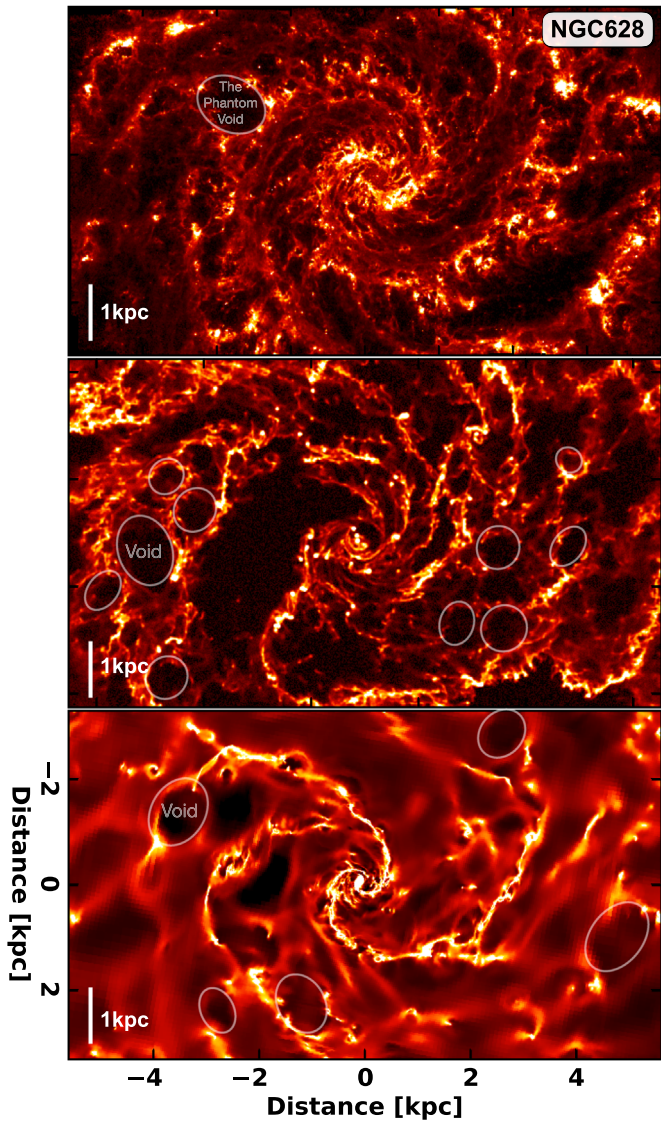


Figure 8. Phantom voids in both observations and simulations. Shown in the upper panel is the JWST 7.7 μm emission map. The middle panel shows the isolated galaxy simulation from Tress et al. (2020; the same simulation shown in the bottom panels of their Figure 14). In color scale is the total column density, which we expect (away from regions of active star formation) to correspond well to the 7.7 μm emission (Leroy et al. 2023; Sandstrom et al. 2023). The bottom panel shows the isolated galaxy simulation tuned for NGC 628 from E. Emsellem et al. (2022, in preparation). We have optimized the color scales such that both maps have a similar qualitative appearance and the physical scales of all panels are matched. We see that large-scale (~ 1 kpc-sized) voids are also common within the simulations, several of which are highlighted by the faded white ellipses.

less in line with the observations, given that the star formation rate contained within the mapped region is $\sim 1 M_{\odot} \text{ yr}^{-1}$. Across the remaining galaxies to be mapped as part of the PHANGS–JWST treasury program (total $42 M_{\odot} \text{ yr}^{-1}$), we could then expect to uncover many phantom voids (albeit these may be harder to identify in galaxies with higher inclinations than NGC 628, because of greater foreground confusion).

We offer a brief comparison between the new JWST observations and theoretical predictions/simulations. Figure 8 compares our 7.7 μm emission map and snapshots from two sets of galaxy simulations (with matched physical scales).

The first is the isolated (noninteracting) galaxy simulation from Tress et al. (2020, 2021). This simulation represents a

generic isolated galaxy and is not tuned to reproduce the particular properties of NGC 628. The aim of the simulation was to study molecular clouds and their associated star formation in a galactic environment. The simulation includes a live N -body stellar and dark matter component. The ISM is modeled using a time-dependent chemical network that keeps track of hydrogen and carbon chemistry, a physically motivated model for the formation of new stars using sink particles, and Type Ia and Type II SN feedback. The simulation reaches subparsec resolution in the dense regions (see Figure 3 in Tress et al. 2020) and self-consistently follows the formation of individual molecular clouds from the large-scale flow and their embedded star formation. More details about the simulation can be found in Tress et al. (2020).

The second simulation is a dedicated hydro-dynamical simulation of an isolated main-sequence star-forming galaxy, using known properties of NGC 628 to generate initial conditions (stellar and gas mass profiles, velocity profile, viewing angles). The simulation was run using Ramses (Teyssier 2002), an adaptive-mesh refinement code with a maximum sampling of 3.6 pc for the gas cells. It includes live particles for dark matter, old and new stars, atomic and molecular cooling, constant efficiency per freefall time star formation above a given gas density, with recipes for UV background, feedback from Type Ia and Type II SNe, radiative pressure, and stellar winds.

The similarity in morphology between simulations and observations is striking. We show as ellipses in the bottom two panels of Figure 8 several large-scale (~ 1 kpc-sized) voids, similar to the Phantom Void, that have been identified in the simulations.⁵⁰ In addition, we see many smaller bubbles in the simulations that are similar in size to the the Precursor Phantom Void. Indeed, simulations have been predicting a bubble-rich ISM morphology for decades (e.g., Wada 2008; Grisdale et al. 2017), and H α observations have hinted at a similar morphology (see, e.g., Figure 1 in Boomsma et al. 2008). However, H α observations have limited resolution outside of the Milky Way, and it is only with the advent of JWST that we can for the first time confirm the predictions of simulations so spectacularly. In simulations which include perturbations from satellites, such as the M51 analog shown in Pettitt et al. (2017), large-scale voids are also clear in the gas column density. The voids seen in Pettitt et al. (2017) are driven by SN feedback, and also track the edges of the spiral arms, as we see in M74. The strong similarity between observations and simulations suggests that the physical processes included in the simulations (gas self-gravity, SN feedback, and differential rotation) are at the origin of the observed morphology. Further analysis, which is out of the scope of this paper, will be necessary to quantify in more detail the statistical properties of simulations versus observations (see, e.g., Sandstrom et al. 2023).

6. Conclusions

This letter demonstrates the potential for new PHANGS–JWST observations to be used to identify (morphologically) stellar-feedback-powered bubbles, and highlights the need for

⁵⁰ We note, however, the identification procedure in the simulations is not identical to the observations (which combined multiple filters). In future, we aim to make a more direct comparison based on, for example, using POLARIS to create synthetic observations of the JWST filters as predicted by the simulation.

multiwavelength data sets to study and understand their physical properties. Here we provide a detailed case study of two regions of interest, one of which contains the most prominent bubble in the galaxy (the Phantom Void, over 1 kpc in diameter), and the other being a smaller region that may be the precursor of the larger bubble (the Precursor Phantom Void). We see that the compact H α typically sits on the edge of the shells, highlighting that the youngest stars are forming at the boundaries of the bubbles, coincident with the youngest (~ 1 Myr) and most massive ($\sim 10^5 M_{\odot}$) HST stellar associations that are also found toward these regions. We also find an older generation (~ 20 Myr) of stellar associations that is present within the bubble of the Phantom Void. From our kinematic analysis of the H I, H $_2$ (CO), and H II gas across the Phantom Void, we infer a high expansion speed of around 15 to 50 km s $^{-1}$. The large size and high expansion speed of the Phantom Void suggest that the driving mechanism is sustained stellar feedback due to multiple mechanisms. We propose a scenario where early feedback first cleared a bubble (as we observe now in the Precursor Phantom Void), and since then SNe have been exploding within this cavity and have accelerated the shell (which can also be enhanced by shear). Finally, comparison to simulations shows a striking resemblance to our JWST observations, and suggest that such massive stellar-feedback-driven bubbles should be common with other galaxies.

We would like to thank the referee for their constructive feedback that helped improve the quality of this paper.

This work was carried out as part of the PHANGS collaboration. This work is based on observations made with the NASA/ESA/CSA JWST and NASA/ESA Hubble Space Telescopes.

Some of the data presented in this paper were obtained from the Mikulski Archive for Space Telescopes (MAST) at the Space Telescope Science Institute, which is operated by the Association of Universities for Research in Astronomy, Inc., under NASA contract NAS 5-03127 for JWST and NASA contract NAS 5-26555 for HST. The JWST observations are associated with program 2107, and those from HST with program 15454. The specific observations analyzed can be accessed via [10.17909/9bdf-jn24](https://doi.org/10.17909/9bdf-jn24) and [10.17909/t9-r08f-dq31](https://doi.org/10.17909/t9-r08f-dq31).

This work also makes use of observations collected at the European Southern Observatory under ESO programmes 094.C-0623 (PI: Kreckel), 095.C-0473, 098.C-0484 (PI: Blanc), 1100.B-0651 (PHANGS–MUSE; PI: Schinnerer), as well as 094.B-0321 (MAGNUM; PI: Marconi), 099.B-0242, 0100.B-0116, 098.B-0551 (MAD; PI: Carollo) and 097.B-0640 (TIMER; PI: Gadotti). This publication uses the data from the AstroSat mission and the UVIT instrument of the Indian Space Research Organisation (ISRO), archived at the Indian Space Science Data center (ISSDC). This work is supported by a grant 19ASTROSA2 from the Canadian Space Agency.

This paper makes use of the following ALMA data: ADS/JAO.ALMA#2012.1.00650.S, ADS/JAO.ALMA#2017.1.00886.L. ALMA is a partnership of ESO (representing its member states), NSF (USA) and NINS (Japan), together with NRC (Canada), MOST and ASIAA (Taiwan), and KASI (Republic of Korea), in cooperation with the Republic of Chile. The Joint ALMA Observatory is operated by ESO, AUI/NRAO and NAOJ.

A.T.B. and F.B. would like to acknowledge funding from the European Research Council (ERC) under the European

Union's Horizon 2020 research and innovation program (grant agreement No. 726384/Empire). E.J.W. acknowledges the funding provided by the Deutsche Forschungsgemeinschaft (DFG, German Research Foundation)—Project-ID 138713538—SFB 881 (“The Milky Way System”, subproject P1). J.P.e. acknowledges support by the DAO ISM grant No. ANR-21-CE31-0010 and by the Programme National “Physique et Chimie du Milieu Interstellaire” (PCMI) of CNRS/INSU with INC/INP, cofunded by CEA and CNES. E.W.K. acknowledges support from the Smithsonian Institution as a Submillimeter Array (SMA) Fellow and the Natural Sciences and Engineering Research Council of Canada. J.M.D.K. gratefully acknowledges funding from the European Research Council (ERC) under the European Union's Horizon 2020 research and innovation program via the ERC Starting Grant MUSTANG (grant No. 714907). COOL Research DAO is a Decentralized Autonomous Organization supporting research in astrophysics aimed at uncovering our cosmic origins. M.C. gratefully acknowledges funding from the DFG through an Emmy Noether Research Group (grant No. CH2137/1-1). R.S.K. acknowledges funding from the European Research Council via the ERC Synergy Grant “ECOGAL” (project ID 855130), from the Deutsche Forschungsgemeinschaft (DFG) via the Collaborative Research Center “The Milky Way System” (SFB 881—funding ID 138713538—subprojects A1, B1, B2, and B8) and from the Heidelberg Cluster of Excellence (EXC 2181-390900948) “STRUCTURES”, funded by the German Excellence Strategy. R.S.K. also thanks the German Ministry for Economic Affairs and Climate Action for funding in the project “MAINN” (funding ID 50OO2206). T.G.W. acknowledges funding from the European Research Council (ERC) under the European Union's Horizon 2020 research and innovation program (grant No. 694343). K.K. and O.E. gratefully acknowledge funding from the Deutsche Forschungsgemeinschaft (DFG, German Research Foundation) in the form of an Emmy Noether Research Group (grant No. KR4598/2-1; PI: Kreckel). G.A.B. acknowledges the support from ANID Basal project FB210003. S.J. is supported by Harvard University through the ITC. M.B. acknowledges support from FONDECYT regular grant 1211000 and by the ANID BASAL project FB210003. E.R. acknowledges the support of the Natural Sciences and Engineering Research Council of Canada (NSERC), funding reference number RGPIN-2022-03499. This research was supported by the Excellence Cluster ORIGINS which is funded by the Deutsche Forschungsgemeinschaft (DFG, German Research Foundation) under Germany's Excellence Strategy—EXC-2094-390783311. Some of the simulations in this paper have been carried out on the computing facilities of the Computational Center for Particle and Astrophysics (C2PAP). E.E. would like to thank Alexey Krukau and Margarita Petkova for their support through C2PAP. K.G. is supported by the Australian Research Council through the Discovery Early Career Researcher Award (DECRA) Fellowship DE220100766 funded by the Australian Government. K.G. is supported by the Australian Research Council Centre of Excellence for All Sky Astrophysics in 3 Dimensions (ASTRO 3D), through project number CE170100013. M.Q. acknowledges support from the Spanish grant No. PID2019-106027GA-C44, funded by MCIN/AEI/10.13039/501100011033. F.R. acknowledges support from the Knut and Alice Wallenberg Foundation. C.E. acknowledges funding from the Deutsche Forschungsgemeinschaft (DFG)

Sachbeihilfe, grant No. BI1546/3-1 A.K.L. gratefully acknowledges support by grant Nos. 1653300 and 2205628 from the National Science Foundation, by award JWST-GO-02107.009-A, and by a Humboldt Research Award from the Alexander von Humboldt Foundation. J.S. acknowledges support by the Natural Sciences and Engineering Research Council of Canada (NSERC) through a Canadian Institute for Theoretical Astrophysics (CITA) National Fellowship.

Facilities: HST (Hubble Space Telescope), JWST, ALMA (Atacama Large Millimeter/submillimeter Array), VLT-MUSE (Very Large Telescope-Multi Unit Spectroscopic Explorer), VLA (The Karl G. Jansky Very Large Array), Spitzer Space Telescope, AstroSat (Astronomy satellite).

Software: Astropy (Astropy Collaboration et al. 2013, 2018, 2022), SAO ImageDS9 (Joye & Mandel 2003), CARTA (Comrie et al. 2021), APIPy (Robitaille & Bressert 2012; Robitaille 2019).

ORCID iDs

Ashley. T. Barnes <https://orcid.org/0000-0003-0410-4504>

Elizabeth J. Watkins <https://orcid.org/0000-0002-7365-5791>

Sharon E. Meidt <https://orcid.org/0000-0002-6118-4048>

Kathryn Kreckel <https://orcid.org/0000-0001-6551-3091>

Mattia C. Sormani <https://orcid.org/0000-0001-6113-6241>

Robin G. Treß <https://orcid.org/0000-0002-9483-7164>

Simon C. O. Glover <https://orcid.org/0000-0001-6708-1317>

Frank Bigiel <https://orcid.org/0000-0003-0166-9745>

Rupali Chandar <https://orcid.org/0000-0003-0085-4623>

Eric Emsellem <https://orcid.org/0000-0002-6155-7166>

Janice C. Lee <https://orcid.org/0000-0002-2278-9407>

Adam K. Leroy <https://orcid.org/0000-0002-2545-1700>

Karin M. Sandstrom <https://orcid.org/0000-0002-4378-8534>

Eva Schinnerer <https://orcid.org/0000-0002-3933-7677>

Erik Rosolowsky <https://orcid.org/0000-0002-5204-2259>

Francesco Belfiore <https://orcid.org/0000-0002-2545-5752>

Guillermo A. Blanc <https://orcid.org/0000-0003-4218-3944>

Médéric Boquien <https://orcid.org/0000-0003-0946-6176>

Jakob den Brok <https://orcid.org/0000-0002-8760-6157>

Yixian Cao <https://orcid.org/0000-0001-5301-1326>

Mélanie Chevance <https://orcid.org/0000-0002-5635-5180>

Daniel A. Dale <https://orcid.org/0000-0002-5782-9093>

Oleg V. Egorov <https://orcid.org/0000-0002-4755-118X>

Cosima Eibensteiner <https://orcid.org/0000-0002-1185-2810>

Kathryn Grasha <https://orcid.org/0000-0002-3247-5321>

Brent Groves <https://orcid.org/0000-0002-9768-0246>

Hamid Hassani <https://orcid.org/0000-0002-8806-6308>

Jonathan D. Henshaw <https://orcid.org/0000-0001-9656-7682>

Sarah Jeffreson <https://orcid.org/0000-0002-4232-0200>

María J. Jiménez-Donaire <https://orcid.org/0000-0002-9165-8080>

Benjamin W. Keller <https://orcid.org/0000-0002-9642-7193>

Ralf S. Klessen <https://orcid.org/0000-0002-0560-3172>

Eric W. Koch <https://orcid.org/0000-0001-9605-780X>

J. M. Diederik Kruijssen <https://orcid.org/0000-0002-8804-0212>

Kirsten L. Larson <https://orcid.org/0000-0003-3917-6460>

Jing Li <https://orcid.org/0000-0002-4825-9367>

- Daizhong Liu <https://orcid.org/0000-0001-9773-7479>
- Laura A. Lopez <https://orcid.org/0000-0002-1790-3148>
- Eric J. Murphy <https://orcid.org/0000-0001-7089-7325>
- Lukas Neumann <https://orcid.org/0000-0001-9793-6400>
- Jérôme Pety <https://orcid.org/0000-0003-3061-6546>
- Francesca Pinna <https://orcid.org/0000-0001-5965-3530>
- Miguel Querejeta <https://orcid.org/0000-0002-0472-1011>
- Florent Renaud <https://orcid.org/0000-0001-5073-2267>
- Toshiiki Saito <https://orcid.org/0000-0001-9016-2641>
- Sumit K. Sarbadhicary <https://orcid.org/0000-0002-4781-7291>
- Amy Sardone <https://orcid.org/0000-0002-5783-145X>
- Rowan J. Smith <https://orcid.org/0000-0002-0820-1814>
- Sophia K. Stuber <https://orcid.org/0000-0002-9333-387X>
- Jiayi Sun <https://orcid.org/0000-0003-0378-4667>
- David A. Thilker <https://orcid.org/0000-0002-8528-7340>
- Antonio Usero <https://orcid.org/0000-0003-1242-505X>
- Bradley C. Whitmore <https://orcid.org/0000-0002-3784-7032>
- Thomas G. Williams <https://orcid.org/0000-0002-0012-2142>

References

- Anand, G. S., Lee, J. C., Van Dyk, S. D., et al. 2021a, *MNRAS*, 501, 3621
- Anand, G. S., Rizzi, L., Tully, R. B., et al. 2021b, *AJ*, 162, 80
- Astropy Collaboration, Price-Whelan, A. M., Lim, P. L., et al. 2022, *ApJ*, 935, 167
- Astropy Collaboration, Price-Whelan, A. M., Sipocz, B. M., et al. 2018, *AJ*, 156, 123
- Astropy Collaboration, Robitaille, T. P., Tollerud, E. J., et al. 2013, *A&A*, 558, A33
- Bagetakos, I., Brinks, E., Walter, F., et al. 2011, *AJ*, 141, 23
- Barnes, A. T., Chandar, R., Kreckel, K., et al. 2022, *A&A*, 662, L6
- Barnes, A. T., Glover, S. C. O., Kreckel, K., et al. 2021, *MNRAS*, 508, 5362
- Barrera-Ballesteros, J. K., Heckman, T., Sanchez, S. F., et al. 2021b, *ApJ*, 909, 131
- Barrera-Ballesteros, J. K., Sánchez, S. F., Heckman, T., et al. 2021a, *MNRAS*, 503, 3643
- Baumgartner, V., & Breitschwerdt, D. 2013, *A&A*, 557, A140
- Bethe, H. A. 1990, *RvMP*, 62, 801
- Bigiel, F., Walter, F., Blitz, L., et al. 2010, *AJ*, 140, 1194
- Blanc, G. A., Weinzierl, T., Song, M., et al. 2013, *AJ*, 145, 138
- Boomsma, R., Oosterloo, T. A., Fraternali, F., van der Hulst, J. M., & Sancisi, R. 2008, *A&A*, 490, 555
- Boquien, M., Burgarella, D., Roehlly, Y., et al. 2019, *A&A*, 622, A103
- Bruzual, G., & Charlot, S. 2003, *MNRAS*, 344, 1000
- Calzetti, D., Lee, J. C., Sabbi, E., et al. 2015, *AJ*, 149, 51
- Chastenet, J., Sutter, J., Sandstrom, K. M., et al. 2023a, *ApJL*, 944, L12
- Chastenet, J., Sutter, J., Sandstrom, K. M., et al. 2023b, *ApJL*, 944, L11
- Chevance, M., Kruijssen, J. M. D., Hygate, A. P. S., et al. 2020, *MNRAS*, 493, 2872
- Chevance, M., Kruijssen, J. M. D., Krumholz, M. R., et al. 2022b, *MNRAS*, 509, 272
- Chevance, M., Krumholz, M. R., McLeod, A. F., et al. 2022a, arXiv:2203.09570
- Chown, R., Li, C., Parker, L., et al. 2021, *MNRAS*, 500, 1261
- Churchwell, E., Povich, M. S., Allen, D., et al. 2006, *ApJ*, 649, 759
- Clarke, C., & Oey, M. S. 2002, *MNRAS*, 337, 1299
- Comrie, A., Wang, K. -S., Hsu, S. -C., et al. 2021, CARTA: The Cube Analysis and Rendering Tool for Astronomy, 2.0.0, Zenodo, doi:10.5281/zenodo.3377984
- Dale, D. A., Cohen, S. A., Johnson, L. C., et al. 2009, *ApJ*, 703, 517
- Dale, J. E., Ercolano, B., & Bonnell, I. A. 2012, *MNRAS*, 424, 377
- Dale, J. E., Ercolano, B., & Bonnell, I. A. 2013, *MNRAS*, 430, 234
- Deger, S., Lee, J., Thilker, D., et al. 2020, AAS Meeting, 235, 178.01
- den Brok, J. S., Chatzigiannakis, D., Bigiel, F., et al. 2021, *MNRAS*, 504, 3221
- Draine, B. T. 2011, *ApJ*, 732, 100
- Draine, B. T., & Li, A. 2007, *ApJ*, 657, 810
- Dutta, P., Begum, A., Bharadwaj, S., & Chengalur, J. N. 2008, *MNRAS*, 384, L34

- Egorov, O., Kreckel, K., Sandstrom, K. M., et al. 2023, *ApJL*, 944, L16
- Elmegreen, B. G., & Lada, C. J. 1977, *ApJ*, 214, 725
- Emsellem, E., Schinnerer, E., Santoro, F., et al. 2022, *A&A*, 659, A191
- Frernali, F. 2017, in Astrophysics and Space Science Library, Gas Accretion onto Galaxies, 430, ed. A. Fox & R. Davé (Berlin: Springer), 323
- Galliano, F., Galametz, M., & Jones, A. P. 2018, *ARA&A*, 56, 673
- Gao, Y., Tan, Q. -H., Gao, Y., et al. 2022, *ApJ*, 940, 133
- Gatto, A., Walch, S., Naab, T., et al. 2017, *MNRAS*, 466, 1903
- Gentry, E. S., Krumholz, M. R., Dekel, A., & Madau, P. 2017, *MNRAS*, 465, 2471
- Grasha, K., Calzetti, D., Adamo, A., et al. 2019, *MNRAS*, 483, 4707
- Grasha, K., Calzetti, D., Bittle, L., et al. 2018, *MNRAS*, 481, 1016
- Grisdale, K., Agertz, O., Romeo, A. B., Renaud, F., & Read, J. I. 2017, *MNRAS*, 466, 1093
- Hannon, S., Lee, J. C., Whitmore, B. C., et al. 2019, *MNRAS*, 490, 4648
- Hannon, S., Lee, J. C., Whitmore, B. C., et al. 2022, *MNRAS*, 512, 1294
- Hassani, H., Rosolowsky, E. W., Leroy, A. K., et al. 2023, *ApJL*, 944, L21
- Heiles, C. 1984, *ApJS*, 55, 585
- Hensley, B. S., & Draine, B. T. 2021, *ApJ*, 906, 73
- Jeffreson, S. M. R., Krumholz, M. R., Fujimoto, Y., et al. 2021, *MNRAS*, 505, 3470
- Joye, W. A., & Mandel, E. 2003, in ASP Conf. Ser. 295, Astronomical Data Analysis Software and Systems XII, ed. H. E. Payne, R. I. Jedrzejewski, & R. N. Hook (San Francisco, CA: ASP), 489
- Kannan, R., Marinacci, F., Simpson, C. M., Glover, S. C. O., & Hernquist, L. 2020, *MNRAS*, 491, 2088
- Keller, B. W., Kruijssen, J. M. D., & Chevance, M. 2022, *MNRAS*, 514, 5355
- Keller, B. W., Wadsley, J., Benincasa, S. M., & Couchman, H. M. P. 2014, *MNRAS*, 442, 3013
- Keller, B. W., Wadsley, J., & Couchman, H. M. P. 2015, *MNRAS*, 453, 3499
- Keller, B. W., Wadsley, J., & Couchman, H. M. P. 2016, *MNRAS*, 463, 1431
- Kennicutt, R. C., Jr., Armus, L., Bendo, G., et al. 2003, *PASP*, 115, 928
- Kim, C.-G., & Ostriker, E. C. 2015, *ApJ*, 802, 99
- Kim, J., Chevance, M., Kruijssen, J. M. D., et al. 2021a, *MNRAS*, 504, 487
- Kim, J., Chevance, M., Kruijssen, J. M. D., et al. 2022b, *MNRAS*, 516, 3006
- Kim, J.-G., Kim, W.-T., & Ostriker, E. C. 2018, *ApJ*, 859, 68
- Kim, J. G., Ostriker, E. C., & Filippova, N. 2021b, *ApJ*, 911, 128
- Krause, M. G. H., Diehl, R., Bagetakos, Y., et al. 2015, *A&A*, 578, A113
- Kruijssen, J. M. D., Schruba, A., Chevance, M., et al. 2019, *Natur*, 569, 519
- Krumholz, M. R., Bate, M. R., Arce, H. G., et al. 2014, in Protostars and Planets VI, ed. H. Beuther et al. (Tucson, AZ: Univ. of Arizona Press), 243
- Lang, P., Meidt, S. E., Rosolowsky, E., et al. 2020, *ApJ*, 897, 122
- Larson, K. L., Lee, J. C., Thilker, D. A., et al. 2023, *MNRAS*, submitted
- Lee, J. C., Whitmore, B. C., Thilker, D. A., et al. 2022, *ApJS*, 258, 10
- Lee, J., Sandstrom, K. M., Leroy, A. K., et al. 2023, *ApJL*, 944, L7
- Leroy, A., Bolatto, A. D., Sandstrom, K. M., et al. 2023, *ApJL*, 944, L9
- Leroy, A. K., Schinnerer, E., Hughes, A., et al. 2021a, *ApJS*, 257, 43
- Leroy, A. K., Hughes, A., Liu, D., et al. 2021b, *ApJS*, 255, 19
- Leroy, A. K., Walter, F., Sandstrom, K., et al. 2013, *AJ*, 146, 19
- Leroy, A. K., Sandstrom, K. M., Lang, D., et al. 2019, *ApJS*, 244, 24
- Li, A. 2020, *NatAs*, 4, 339
- Mac Low, M. -M., & McCray, R. 1988, *ApJ*, 324, 776
- Martizzi, D., Faucher-Giguère, C. -A., & Quataert, E. 2015, *MNRAS*, 450, 504
- McKee, C. F., & Ostriker, J. P. 1977, *ApJ*, 218, 148
- McLeod, A. F., Ali, A. A., Chevance, M., et al. 2021, *MNRAS*, 508, 5425
- Nath, B. B., Das, P., & Oey, M. S. 2020, *MNRAS*, 493, 1034
- Oey, M. S., & Clarke, C. J. 1997, *MNRAS*, 289, 570
- Orr, M. E., Fielding, D. B., Hayward, C. C., & Burkhardt, B. 2022, *ApJL*, 924, L28
- Palous, J., Franco, J., & Tenorio-Tagle, G. 1990, *A&A*, 227, 175
- Pettitt, A. R., Tasker, E. J., Wadsley, J. W., Keller, B. W., & Benincasa, S. M. 2017, *MNRAS*, 468, 4189
- Pineda, J. E., Arzoumanian, D., André, P., et al. 2022, arXiv:2205.03935
- Querejeta, M., Meidt, S. E., Schinnerer, E., et al. 2015, *ApJS*, 219, 5
- Rahner, D., Pellegrini, E. W., Glover, S. C. O., & Klessen, R. S. 2017, *MNRAS*, 470, 4453
- Rahner, D., Pellegrini, E. W., Glover, S. C. O., & Klessen, R. S. 2019, *MNRAS*, 483, 2547
- Raskutti, S., Ostriker, E. C., & Skinner, M. A. 2016, *ApJ*, 829, 130
- Regan, M. W., Thornley, M. D., Vogel, S. N., et al. 2006, *ApJ*, 652, 1112
- Robitaille, T. 2019, APLpy v2.0: The Astronomical Plotting Library in Python, Zenodo, doi:10.5281/zenodo.2567476
- Robitaille, T., & Bressert, E. 2012, APLpy: Astronomical Plotting Library in Python, Astrophysics Source Code Library, ascl:1208.017
- Sandstrom, K., Koch, E. W., Leroy, A. K., et al. 2023, *ApJL*, 944, L8
- Sharma, P., Roy, A., Nath, B. B., & Shchekinov, Y. 2014, *MNRAS*, 443, 3463
- Simpson, R. J., Povich, M. S., Kendrew, S., et al. 2012, *MNRAS*, 424, 2442
- Smith, J. D. T., Draine, B. T., Dale, D. A., et al. 2007, *ApJ*, 656, 770
- Sun, J., Leroy, A. K., Ostriker, E. C., et al. 2020, *ApJ*, 892, 148
- Tamburro, D., Rix, H. W., Leroy, A. K., et al. 2009, *AJ*, 137, 4424
- Teyssier, R. 2002, *A&A*, 385, 337
- Thornton, K., Gaudlitz, M., Janka, H. T., & Steinmetz, M. 1998, *ApJ*, 500, 95
- Tress, R. G., Smith, R. J., Sormani, M. C., et al. 2020, *MNRAS*, 492, 2973
- Tress, R. G., Sormani, M. C., Smith, R. J., et al. 2021, *MNRAS*, 505, 5438
- Veilleux, S., Cecil, G., & Bland-Hawthorn, J. 2005, *ARA&A*, 43, 769
- Wada, K. 2008, *ApJ*, 675, 188
- Walter, F., Brinks, E., de Blok, W. J. G., et al. 2008, *AJ*, 136, 2563
- Watkins, E., Barnes, A., Henny, K. F., et al. 2023, *ApJL*, 944, L24
- Watson, C., Povich, M. S., Churchwell, E. B., et al. 2008, *ApJ*, 681, 1341
- Weaver, R., McCray, R., Castor, J., Shapiro, P., & Moore, R. 1977, *ApJ*, 218, 377
- Weisz, D. R., Skillman, E. D., Cannon, J. M., et al. 2009a, *ApJ*, 704, 1538
- Weisz, D. R., Skillman, E. D., Cannon, J. M., et al. 2009b, *ApJL*, 691, L59
- Whitworth, A. P., Bhattacharyya, A. S., Chapman, S. J., Disney, M. J., & Turner, J. A. 1994, *MNRAS*, 268, 291
- Zucker, C., Goodman, A. A., Alves, J., et al. 2022, *Natur*, 601, 334